

# Molecular architecture of the chick vestibular hair bundle

Jung-Bum Shin<sup>1,2,8</sup>, Jocelyn F Krey<sup>2,8</sup>, Ahmed Hassan<sup>3</sup>, Zoltan Metlagel<sup>3</sup>, Andrew N Tauscher<sup>3</sup>, James M Pagana<sup>1,2</sup>, Nicholas E Sherman<sup>4</sup>, Erin D Jeffery<sup>4</sup>, Kateri J Spinelli<sup>2</sup>, Hongyu Zhao<sup>2</sup>, Phillip A Wilmarth<sup>5</sup>, Dongseok Choi<sup>6</sup>, Larry L David<sup>5</sup>, Manfred Auer<sup>3</sup> & Peter G Barr-Gillespie<sup>2,7</sup>

Hair bundles of the inner ear have a specialized structure and protein composition that underlies their sensitivity to mechanical stimulation. Using mass spectrometry, we identified and quantified >1,100 proteins, present from a few to 400,000 copies per stereocilium, from purified chick bundles; 336 of these were significantly enriched in bundles. Bundle proteins that we detected have been shown to regulate cytoskeleton structure and dynamics, energy metabolism, phospholipid synthesis and cell signaling. Three-dimensional imaging using electron tomography allowed us to count the number of actin-actin cross-linkers and actin-membrane connectors; these values compared well to those obtained from mass spectrometry. Network analysis revealed several hub proteins, including RDX (radixin) and SLC9A3R2 (NHERF2), which interact with many bundle proteins and may perform functions essential for bundle structure and function. The quantitative mass spectrometry of bundle proteins reported here establishes a framework for future characterization of dynamic processes that shape bundle structure and function.

An outstanding example of a specialized organelle devoted to a single purpose, the vertebrate hair bundle transduces mechanical signals for the inner ear, converting sound and head movement to electrical signals that propagate to the central nervous system. Protruding from the apical surface of a sensory hair cell, a bundle typically consists of 50–100 actin-filled stereocilia and, at least during development, an axonemal kinocilium<sup>1</sup>. A bundle enlists ~100 transduction channels, which are mechanically gated by tip links as external forces oscillate the bundle; the opening and closing of the channels in turn modulates the hair cell's membrane potential, controlling neurotransmitter release.

Because hair bundles have a reduced protein complement and carry out a specialized task, once we know which proteins are present—as well as their concentrations and interactions—understanding bundles' assembly and operation seems possible. Although genetics studies have identified many proteins essential for bundle function<sup>2</sup>, others may have escaped detection because they are essential during development or, in some cases, can be compensated for by paralogs. To discover these additional proteins, biochemical strategies are essential. Although bundles are scarce, quantitative mass spectrometry<sup>3</sup> has the sensitivity and accuracy to detect and quantify the bundle's protein complement.

Our previous analysis of hair-bundle proteins using mass spectrometry detected 59 proteins, including several that are critical for bundle function<sup>4</sup>. Here, using a more sensitive mass spectrometer, we detected over 1,100 proteins from chick vestibular bundles and

identified those proteins selectively targeted to bundles. Many bundle-enriched proteins are expressed from deafness-associated genes, confirming their essential function in the inner ear. We also imaged stereocilia using electron tomography and counted actin-actin cross-linkers and actin-membrane connectors; those counts compared favorably to mass-spectrometric estimates for cross-linker and connector proteins. To place the bundle's proteome into a network of functional and structural interactions, we assembled an interaction map that highlights the central roles in hair-bundle function played by actin, phosphatidylinositol-4,5-bisphosphate (PtdIns(4,5)P<sub>2</sub>), Ca<sup>2+</sup> and CALM (calmodulin). Moreover, we identified two other key hub proteins: the ezrin-radixin-moesin (ERM) family member RDX (radixin), important in hair-bundle function<sup>5</sup>, and SLC9A3R2 (NHERF2; solute carrier family 9 member 3 regulator 2), a PDZ-domain adaptor protein that couples RDX to many transmembrane proteins<sup>6</sup>. The comprehensive view offered by quantitative mass spectrometry reveals functional pathways in hair bundles and, on the basis of the absence of key protein families, also rules out alternative mechanisms.

## RESULTS

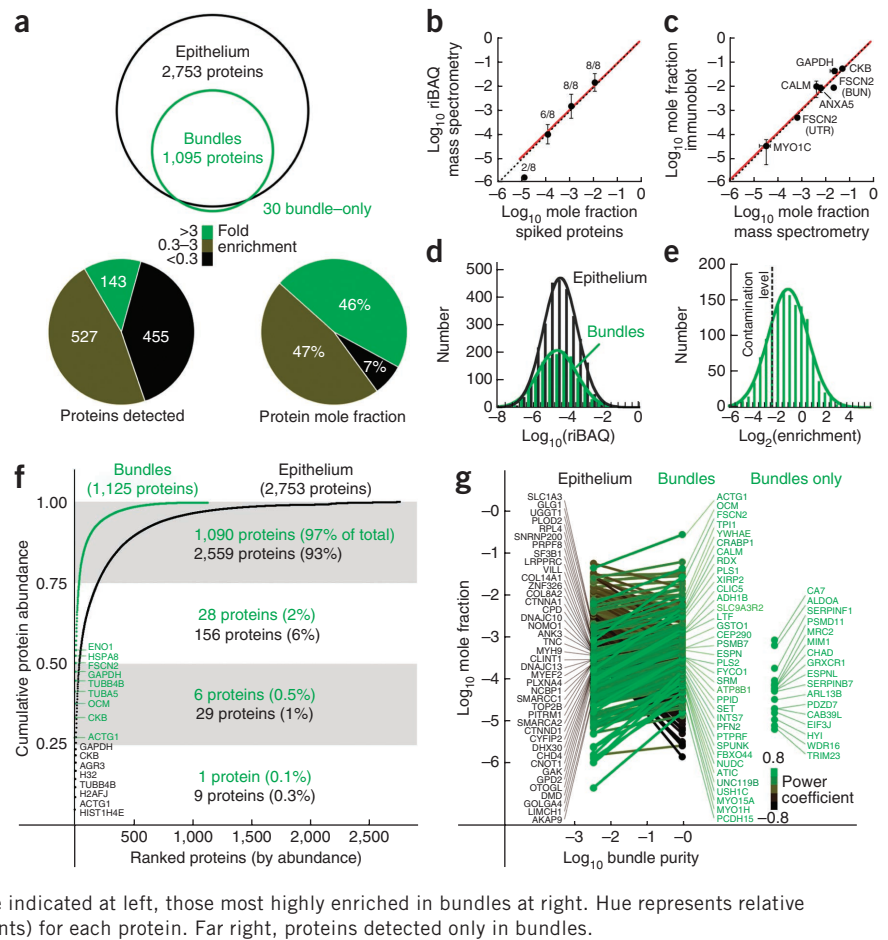
### Mass spectrometry of purified hair bundles

Using liquid-chromatographic tandem mass spectrometry (LC-MS/MS), we identified proteins from hair bundles and epithelia of utricles (Supplementary Fig. 1), vestibular organs that detect linear acceleration, from embryonic day 20–21 chicks; at this age, utricles are functional<sup>7</sup>. Bundles (BUN) were enriched 40-fold, to ~80% purity

<sup>1</sup>Department of Neuroscience, University of Virginia, Charlottesville, Virginia, USA. <sup>2</sup>Oregon Hearing Research Center, Oregon Health & Science University, Portland, Oregon, USA. <sup>3</sup>Life Sciences Division, Lawrence Berkeley National Laboratory, Berkeley, California, USA. <sup>4</sup>W.M. Keck Biomedical Mass Spectrometry Laboratory, University of Virginia, Charlottesville, Virginia, USA. <sup>5</sup>Department of Biochemistry & Molecular Biology, Oregon Health & Science University, Portland, Oregon, USA. <sup>6</sup>Department of Public Health & Preventive Medicine, Oregon Health & Science University, Portland, Oregon, USA. <sup>7</sup>Vollum Institute, Oregon Health & Science University, Portland, Oregon, USA. <sup>8</sup>These authors contributed equally to this work. Correspondence should be addressed to P.G.B.-G. (gillespp@ohsu.edu).

Received 20 August 2012; accepted 17 December 2012; published online 20 January 2013; doi:10.1038/nn.3312

**Figure 1** Quantitative analysis of chick hair-bundle proteins. **(a)** Top, proteins identified in bundles and epithelium (two or more experiments). Bottom left, representation of bundle proteins as bundle-enriched, unenriched and epithelium-enriched (by protein frequency). Bottom right, same as left except with the mole fractions of proteins in each class summed. **(b)** Calibration curve relating mole fraction of human protein standards spiked into *E. coli* extract to riBAQ value. The number of identified proteins is indicated for each data point (mean  $\pm$  s.d.). The points corresponding to mole fractions of  $10^{-2}$ ,  $10^{-3}$  and  $10^{-4}$  were fit with a line constrained through the origin ( $y = 1.02x$ ;  $R = 0.999$ ). **(c)** Calibration curve relating mole fraction determined from riBAQ values to mole fraction measured using quantitative immunoblots with purified proteins as standards; data points are mean  $\pm$  s.e.m. and are fit by  $y = 0.98x$  ( $R = 0.97$ ). Data for CKB and GAPDH were from ref. 4. Dotted lines in **a, b** correspond to unity. **(d)** Abundance distribution of bundle and epithelium proteins; single Gaussian fits. **(e)** Enrichment distribution of proteins detected in bundles and epithelium; single Gaussian fit. **(f)** Cumulative protein molar abundance, from highest to lowest. The most abundant proteins in bundles and epithelium are indicated. **(g)** Mole fractions of proteins in epithelium (left) and bundle (right); the slope of the line connecting them represents bundle-to-epithelium enrichment.



Proteins most highly enriched in the epithelium are indicated at left, those most highly enriched in bundles at right. Hue represents relative enrichment (power coefficient of fit connecting points) for each protein. Far right, proteins detected only in bundles.

(see below), using the twist-off technique<sup>4,8</sup>. To obtain utricular epithelia (UTR), we used an eyelash to peel the hair-cell and supporting-cell layer from the underlying stroma layer (**Supplementary Fig. 1b**). Four experiments each of BUN and UTR were analyzed.

We identified proteins using an Orbitrap mass spectrometer, analyzing data with the Andromeda search engine and MaxQuant<sup>9,10</sup>. Proteins that shared more than 20% of their detected peptides were combined into protein groups, which were denoted by their best scoring member. We identified a total of 2,944 proteins or protein groups in the union of BUN and UTR. Increasing stringency by only considering proteins found in two or more experiments, we identified 1,125 proteins from bundles (**Fig. 1a** and **Supplementary Table 1**); 728 were identified in all four experiments. Only 20 proteins (<2%) were identified with a single unique peptide. In utricular epithelia, we identified 2,753 proteins in two or more experiments, including 2,147 in all four experiments.

**Quantification using relative iBAQ values**

To quantify hair-bundle proteins, we used the iBAQ algorithm, which divides the sum of all precursor-peptide intensities by the number of theoretically observable peptides<sup>11</sup>. We normalized each protein's iBAQ value to the sum of all iBAQ values, generating a relative iBAQ (riBAQ) value for each protein. Although a previous report demonstrated the linearity of the iBAQ approach<sup>11</sup>, we sought a more rigorous validation: does riBAQ accurately report the mole fraction of each protein? We mimicked experiments with complex protein mixtures by detecting human proteins diluted in an *Escherichia coli* extract as a protein background. Only the more abundant human proteins

were detected, demonstrating the limitations in detecting proteins at low mole fractions. We carried out a linear regression ( $\text{log}_{10}$  riBAQ =  $1.02 \pm 0.01 \times \text{log}_{10}$  mole fraction) with the  $10^{-2}$ ,  $10^{-3}$  and  $10^{-4}$  mole fraction data points (**Fig. 1b**). Although the  $10^{-5}$  data point did not fall on the regression line, only two of eight proteins were detected. We conclude that the correspondence between riBAQ and mole fraction is nearly exact, at least above to a mole fraction of  $\sim 10^{-5}$  (**Fig. 1b**).

To independently verify our riBAQ calibration, we measured the concentrations of five hair-bundle proteins using quantitative immunoblotting (**Fig. 1c**). We only used proteins for which we had purified protein standards, which allowed us to generate accurate standard curves with known amounts of protein. The fit was very close to 1:1 ( $y = 0.98x$ ;  $R = 0.97$ ), confirming that riBAQ values reported mole fraction accurately.

**Quantification of hair-bundle proteins**

With knowledge of total number of molecules per stereocilium, or of molecules per stereocilium of one accurately measured protein, mole fraction values can be used to estimate the number of molecules per stereocilium for any protein. Because actin monomers are present at minimal levels in stereocilia<sup>8</sup> and because each stereocilium has 400,000 filamentous actin molecules (by electron tomography; see below), we used this estimate and actin's mole fraction value to convert mole fraction values for each hair bundle protein into molecules per stereocilium (**Supplementary Table 1**). The distribution of protein abundance values was similar for hair-bundle and epithelium proteins (**Fig. 1d**), indicating that low-abundance proteins were similarly detected in both preparations.



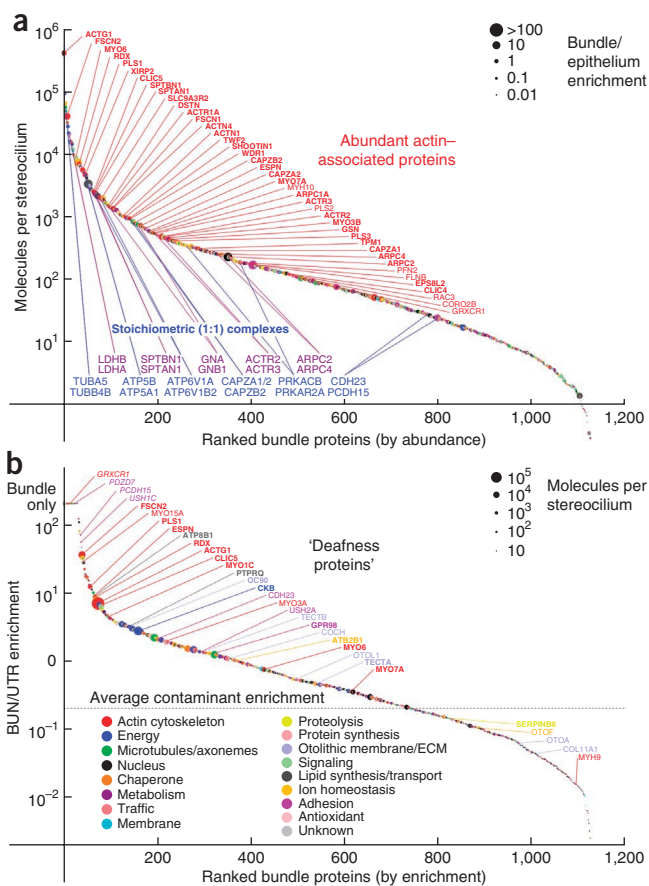
**Figure 2** Protein composition of chick hair bundles. **(a)** Hair bundle proteins ranked in order of abundance. Data-point color indicates protein class (key in panel **b**); symbol size represents bundle-to-epithelium enrichment. Red callouts indicate the most abundant actin-associated proteins; proteins significantly enriched ( $P < 0.05$ ) over the contamination fraction are indicated by boldface symbols. Blue and magenta callouts highlight proteins known to be in 1:1 stoichiometry. **(b)** Bundle proteins ranked in order of enrichment. Color indicates protein class; symbol size indicates abundance. Proteins encoded by deafness-associated genes are indicated; deafness-linked proteins significantly enriched ( $P < 0.05$ ) over the contamination fraction are indicated by boldface symbols, those detected in two or fewer epithelium runs (hence not subject to statistical analysis) are indicated by italic symbols.

Proteins that are selectively targeted to hair bundles may be particularly important for function. Given that bundles constitute ~2% of the epithelium (Online Methods), targeted proteins could have a bundle-to-epithelium ratio (enrichment) as large as 50-fold. Because stereocilia are not closed compartments, however, diffusible cell-body proteins will also be present in bundles, with an enrichment of ~1. Finally, the bundle preparation will also contain cell-body contaminants. The broad histogram of binned enrichment values reflected the presence of all three types of proteins (**Fig. 1e**).

We determined the contamination fraction, the average BUN/UTR ratio for proteins known not to be in stereocilia, by measuring relative molar abundances of proteins from mitochondria and nuclei, which are absent from stereocilia<sup>12</sup>. We chose 81 nuclear and mitochondrial proteins detected in three or more utricle experiments; proteins that were not detected in bundles were assigned an enrichment value of 0. The contamination fraction estimated from these 81 proteins was  $0.20 \pm 0.25$  (mean  $\pm$  s.d.), which suggests that the BUN preparation contains ~80% hair bundles; bundles were thus purified approximately 40-fold.

To validate the estimated contamination fraction, we used quantitative immunoblotting (**Supplementary Figs. 2a,b** and 3) to measure the presence in the BUN sample of five proteins known to be absent from hair bundles: ATP1A1 (ATPase, Na<sup>+</sup>/K<sup>+</sup> transporting, alpha 1 polypeptide), found on the basolateral membranes of hair cells and supporting cells<sup>13</sup>; HSPA5 (heat shock protein 5; GRP78), an endoplasmic reticulum marker; MDH2 (malate dehydrogenase 2), a component of the mitochondrial citric acid cycle; PTPRJ (protein tyrosine phosphatase receptor J, also known as the supporting cell antigen), present on supporting cell apical surfaces<sup>14</sup>; and VIM (vimentin), an intermediate filament protein found in cell bodies of hair cells and supporting cells of the vestibular system<sup>15</sup>. Using immunocytochemistry, we confirmed that these proteins are absent from hair bundles (**Supplementary Fig. 2c**). As controls, we also examined actin and FSCN2 by immunoblotting (**Supplementary Fig. 2a**); each is concentrated in hair bundles (**Supplementary Fig. 2c**). In 14 measurements from 6 sets of BUN and UTR samples, we measured a contamination fraction of  $0.30 \pm 0.14$  (mean  $\pm$  s.d.), similar to that estimated by mass spectrometry. As further confirmation of the bundle enrichment of proteins detected in our analysis, we observed appropriate distribution of 16 bundle proteins by immunocytochemistry and 14 bundle proteins by immunoblotting (**Supplementary Figs. 4** and 5).

We used riBAQ measurement errors, propagated in combination with the error in the calibration slope measurement, to estimate errors in protein enrichment and abundance reported in **Supplementary Table 1**. To determine the slope error, we plotted log<sub>10</sub> riBAQ against log<sub>10</sub> mole fraction (reversed axes from **Fig. 1b**) for all human proteins detected in the 10<sup>-2</sup>–10<sup>-4</sup> mole fraction range. We used a linear mixed-effects model to generate a fit through the data,



constrained through the origin; the slope of the calibration curve was  $1.00 \pm 0.03$ . Using the contamination fraction and the mole fraction of each protein in hair-bundle and epithelium samples, we corrected the abundance of each protein to reflect its actual concentration in bundles (**Supplementary Table 1**). Because of the substantial uncertainty in the contamination fraction, these corrected values are much more reliable for bundle-enriched proteins.

The most abundant proteins in hair bundles included ACTG1 (gamma actin, representing all actins), CKB (brain creatine kinase), OCM (parvalbumin CPV3), TUBA5 and TUBB4B (representing all alpha and beta tubulins) and FSCN2 (fascin 2) (**Fig. 1f**). Glycolytic enzymes were abundant, as were HSPA8 and HSP90AA1 (representing the 70 and 90 kDa heat shock protein families). Only seven proteins (0.6%) accounted for 50% of the total proteome molar abundance in bundles (**Fig. 1f**).

We highlighted proteins with high bundle or epithelium enrichment, plotting mole fraction for all proteins detected in both samples against approximate bundle purity (**Fig. 1g**). Some proteins were only identified in bundles—for example, PDZD7 (PDZ domain containing 7)<sup>16</sup>—presumably because their epithelium concentration is below the limit of detection. We may have underestimated the hair-bundle riBAQ values for high-molecular-mass proteins, however. Because we carried out strong cation exchange (SCX) purification only for BUN gel slices that were adjacent to sample wells (Online Methods), recovery of proteins from these slices may have been less efficient than from the corresponding UTR slices. Consequently, our estimates of concentrations and enrichment values for CDH23 (cadherin 23), GPR98 (VLGR1; G-protein coupled receptor 98) and USH2A (usherin), all of which are especially large, may be too low.



We used the contamination fraction to determine which proteins were reliably present in hair bundles. Of the 1,095 proteins detected in two or more experiments each of bundles and epithelium, 336 had a

bundle-to-epithelium enrichment higher than the contamination fraction with a *P* value <0.05, adjusted for the false-discovery rate (FDR), the rate of incorrect assignments among enriched proteins<sup>17</sup>. Many

**Table 1 Quantification of actin and actin-binding proteins in chick stereocilia**

Identifier or protein group	Description	Protein symbol	Group members	Paralog in BUN?	BUN/UTR ratio	Corrected molecules per SC
ACT	Actin gamma 1	ACTG1	ACTG1, ACTA1, ACTA2, ACTB, ACTBL2, ACTC1, ACTG2	Yes	7	400,000
NP_001171209	<b>Fascin 2</b>	<b>FSCN2</b>	<b>FSCN2</b>	<b>Yes</b>	<b>40</b>	<b>40,000</b>
ERM	<b>Radixin</b>	<b>RDX</b>	<b>RDX, EZR, MSN</b>	<b>Yes</b>	<b>9</b>	<b>6,800</b>
ENSGALP00000025573	Myosin VI	MYO6	MYO6	No	0.8	6,600
ENSGALP00000004164	<b>Plastin 1</b>	<b>PLS1</b>	<b>PLS1</b>	<b>Yes</b>	<b>12</b>	<b>5,500</b>
ENSGALP00000017765	Xin actin-binding repeat-containing protein 2	XIRP2	XIRP2	Yes	13	4,600
ENSGALP00000030892	Chloride intracellular channel 5	CLIC5	CLIC5	Yes	6	2,400
ENSGALP00000008988	Solute carrier family 9 member 3 regulator 2	SLC9A3R2	SLC9A3R2	No	17	2,000
SPTAN1	Spectrin, alpha, non-erythrocytic 1	SPTAN1	SPTAN1	No	0.5	1,400
NP_001171603	<b>Fascin 1</b>	<b>FSCN1</b>	<b>FSCN1</b>	<b>Yes</b>	<b>4</b>	<b>1,300</b>
ENSGALP00000013109	ARP1 actin-related protein 1 homolog A, centractin alpha	ACTR1A	ACTR1A	No	1.7	1,300
ENSGALP00000014097	Destrin (actin depolymerizing factor)	DSTN	DSTN	No	1.3	1,300
ENSGALP00000013240	Spectrin, beta, non-erythrocytic 1	SPTBN1	SPTBN1	No	0.4	1,300
ENSGALP00000023085	Actinin, alpha 4	ACTN4	ACTN4	Yes	1.4	1,100
TWF2	Twinfilin-2	TWF2	TWF2, TWF2/WDR82	No	4	950
ENSGALP00000015053	Shootin-1	SHOOTIN1	SHOOTIN1	No	5	910
ENSGALP00000036480	WD repeat domain 1	WDR1	WDR1	No	3	870
ACTN1/2	Actinin, alpha 1	ACTN1	ACTN1, ACTN2	Yes	0.9	790
XP_417532.3	<b>Espin</b>	<b>ESPN</b>	<b>ESPN</b>	<b>Yes</b>	<b>10</b>	<b>710</b>
ENSGALP00000006414	Capping protein, beta 2	CAPZB2	CAPZB2, CAPZB1	No	2	690
ENSGALP00000015277	Capping protein, alpha 2	CAPZA2	CAPZA2	Yes	1.3	540
ENSGALP00000007451	Actin related protein 2/3 complex, subunit 1A, 41 kDa	ARPC1A	ARPC1A, ARPC1B	Yes	1.2	470
ENSGALP00000027391	<b>Plastin 2</b>	<b>PLS2</b>	<b>PLS2</b>	<b>Yes</b>	<b>21</b>	<b>460</b>
ENSGALP00000015632	Myosin IIIB	MYO3B	MYO3B	Yes	4	430
ENSGALP00000038669	ARP2 actin-related protein 2 homolog	ACTR2	ACTR2	Yes	2	430
ENSGALP00000009526	<b>Plastin 3</b>	<b>PLS3</b>	<b>PLS3</b>	<b>Yes</b>	<b>3</b>	<b>400</b>
ENSGALP00000019832	ARP3 actin-related protein 3 homolog	ACTR3	ACTR3, ACTR3B	Yes	0.7	400
TPM1/3	Tropomyosin 1	TPM1	TPM1, TPM3	Yes	4	300
ENSGALP00000039390	Capping protein, alpha 1	CAPZA1	CAPZA1	Yes	2	260
ENSGALP00000001044	Myosin VIIA	MYO7A	MYO7A	No	0.3	250
ENSGALP00000010800	Actin related protein 2/3 complex, subunit 4, 20 kDa	ARPC4	ARPC4		1.1	210
ENSGALP00000002197	Gelsolin	GSN	GSN	No	0.4	190
ENSGALP00000038130	Profilin 2	PFN2	PFN2	No	5	180
ENSGALP00000018652	Actin related protein 2/3 complex, subunit 2, 34 kDa	ARPC2	ARPC2	No	1.7	180
ENSGALP00000039755	EPS8-like 2	EPS8L2	EPS8L2	No	0.97	130
RAC	Ras-related C3 botulinum toxin substrate 3	RAC3	RAC3, RAC1, RAC2, RHOG	No	1.8	130
ENSGALP00000001914	Chloride intracellular channel 4	CLIC4	CLIC4, CLIC6	Yes	1.0	100
ENSGALP00000001794	Myosin, heavy chain 10, non-muscle	MYH10	MYH10, MYH1	Yes	0.2	95
ENSGALP00000010106	<b>Espin-like</b>	<b>ESPNL</b>	<b>ESPNL</b>	<b>Yes</b>	<b>BUN only</b>	<b>91</b>
ENSGALP00000036676	Glutaredoxin, cysteine rich 1	GRXCR1	GRXCR1	No	BUN only	81
ENSGALP00000013036	Coronin, actin binding protein, 2B	CORO2B	CORO2B	Yes	0.9	69
ENSGALP00000007931	Synapsin I	SYN1	SYN1	Yes	1.0	65
ENSGALP00000007959	Myosin XVA	MYO15A	MYO15A	No	34	50
ENSGALP00000008214	Myosin IC	MYO1C	MYO1C	Yes	6	47
ENSGALP00000008212	Myosin IH	MYO1H	MYO1H	Yes	16	46
ENSGALP00000001365	Huntingtin interacting protein 1	HIP1	HIP1	No	0.4	36
ENSGALP000000039629	Vinculin	VCL	VCL	No	0.4	31
EBP41/L3	Erythrocyte membrane protein band 4.1	EPB41	EPB41, EPB41L3	Yes	0.7	24
ENSGALP00000022935	Coronin, actin binding protein, 1C	CORO1C	CORO1C	Yes	1.3	19
ENSGALP00000019631	Actin-related protein 10 homolog (ARP11)	ACTR10	ACTR10	Yes	0.9	18
ENSGALP00000017268	Mediator of cell motility 1	MEMO1	MEMO1	No	0.5	9
ENSGALP00000027304	LIM domain 7	LMO7	LMO7	No	1.3	6
ACTL6A	Actin-like 6A (ARP4)	ACTL6A	ACTL6A	No	0.2	5
ENSGALP00000012361	Myosin IIIA	MYO3A	MYO3A	Yes	2.7	4
ENSGALP00000009946	LIM domain and actin binding 1	LIMA1	LIMA1	Yes	0.3	3
ENSGALP00000007644	Myosin phosphatase Rho interacting protein	MPRIP	MPRIP	No	0.2	1

Identifier or protein group column gives the Ensembl or NCBI identifier, or experimentally assigned protein group name; description column gives the common name of the principal entry, the protein with most mass-spectrometric evidence; protein symbol is the official protein symbol (based on human genes); group members lists symbols for all proteins in bundles that are summed together in an entry (alphabetical order after principal entry); paralog in BUN indicates whether a paralog is present in bundles; BUN/UTR ratio indicates the bundle/utricle enrichment; corrected molecules per SC is the estimated molecules per stereocilium, determined with ribAQ quantification and corrected for enrichment. Actin cross-linking proteins are indicated in bold; the predominant actin-to-membrane connector family is indicated in underlined bold.



**Table 2 Candidates for mapped but uncloned deafness-associated genes**

Human deafness locus	Chicken protein identifier	Homologous human gene	Chr	Description	Protein symbol	BUN/UTR ratio
AUNA1	ENSGALP00000027391	ENSG00000136167	13	Plastin 2	PLS2	21
AUNA1	ENSGALP00000027417	ENSG00000102547	13	Calcium binding protein 39-like	CAB39L	Bundle only
DFNA16	ENSGALP00000015632	ENSG00000071909	2	Myosin IIIB	MYO3B	3
DFNA18	ENSGALP00000004164	ENSG00000120756	3	Plastin 1	PLS1	4
DFNA32	ENSGALP00000039755	ENSG00000177106	11	Epidermal growth factor receptor kinase substrate 8-like protein 2	EPS8L2	1
DFNB55	ENSGALP00000022269	ENSG00000128050	4	Multifunctional protein ADE2	PAICS	1
DFNB55	ENSGALP00000022326	ENSG00000109265	4	Uncharacterized protein KIAA1211	KIAA1211	3
DFNB57	ENSGALP00000013870	ENSG00000108039	10	Xaa-Pro aminopeptidase 1	XPNPEP1	3
DFNB57	ENSGALP00000015053	ENSG00000187164	10	Shootin-1	SHOOTIN1	5
DFNB57	ENSGALP00000032553	ENSG00000186862	10	PDZ domain containing 7	PDZD7	Bundle only
DFNB85	ENSGALP00000007825	ENSG00000175662	17	TOM1-like protein 2	TOM1L2	1
DFNX5	ENSGALP00000009526	ENSG00000102024	X	Plastin 3	PLS3	3
DFNX5	ENSGALP00000031748	ENSG00000165704	X	Hypoxanthine-guanine phosphoribosyl-transferase	HPRT	4

The human deafness locus column gives the unmapped human deafness locus identifier; chick protein identifier is the chicken Ensembl identifier for the gene encoding the protein mapping to a human deafness-associated gene; homologous human gene is the Ensembl identifier for the human gene to which a given chick protein maps; Chr is the human chromosome; description gives the descriptive name for the protein; BUN/UTR ratio is the bundle/utricle enrichment in chick.

actin-associated proteins were present at 100 or more copies per stereocilium (Fig. 2a and Table 1). Moreover, proteins known to be in 1:1 stoichiometric complexes were present at the expected relative abundances (Fig. 2a), which independently corroborated our quantification.

### 'Deafness proteins' are enriched in hair bundles

We ranked proteins by bundle enrichment and labeled those proteins encoded by deafness- or vestibular-dysfunction-associated genes (Fig. 2b). A list of 7,112 Online Mendelian Inheritance in Man (OMIM) terms and their mapping to human genes and MGI marker accession IDs (downloaded October 2012) was used to identify deafness-associated proteins in the list of proteins identified from BUN and UTR samples, including redundant proteins present in protein groups (Supplementary Table 1). We used two terms to search the OMIM data: "deafness" and "Usher syndrome."

Most deafness-associated proteins detected were enriched in hair bundles; 4% of the 277 proteins enriched >2-fold were associated with deafness in the OMIM database<sup>18</sup>, compared to only 0.7% of 2,667 proteins enriched <2-fold ( $P < 10^{-4}$ , Fisher's exact test). The OMIM database has 163 entries annotated with deafness or Usher syndrome, corresponding to 0.7% of the ~23,500 genes in the human Ensembl database. Proteins enriched >2-fold were also significantly ( $P < 10^{-2}$ ) associated with mouse deafness entries in the Mouse Genome Database (MGD)<sup>19</sup>. The list of proteins enriched in bundles over epithelium is thus a rich reference for proteins with demonstrated significance for auditory and vestibular function.

The OMIM and MGI databases do not include all genes associated with deafness or vestibular dysfunction that are expressed in stereocilia. Adding other known deafness proteins (Supplementary Table 1), including those implicated by means of targeted mutagenesis, our mass spectrometry experiments detected 22 of 27 mouse deafness-associated proteins known to be expressed in stereocilia<sup>2</sup>. These 22 proteins had an average bundle-to-epithelium enrichment of  $29 \pm 12$  (mean  $\pm$  s.e.m.), confirming that the enrichment analysis successfully identified functionally important proteins. Only DFNB31 (whirlin), CLRN1 (clarin 1), LHFPL5 (TMHS; lipoma HMGIC fusion partner-like 5), USH1G (Sans) and STRC (stereocilin) were not detected. Two of these proteins we did not expect to detect: USH1G transcripts are undetectable in embryonic day 20–21 utricles<sup>20</sup>, accounting for the absence of the protein, and STRC is not present in the chick Ensembl database, so cannot be detected with our mass spectrometric approach. Thus only about 10% of known, detectable

stereocilia deafness-associated proteins (3 of 25) escaped observation by mass spectrometry, either because of their low abundance or because they are in auditory but not vestibular stereocilia.

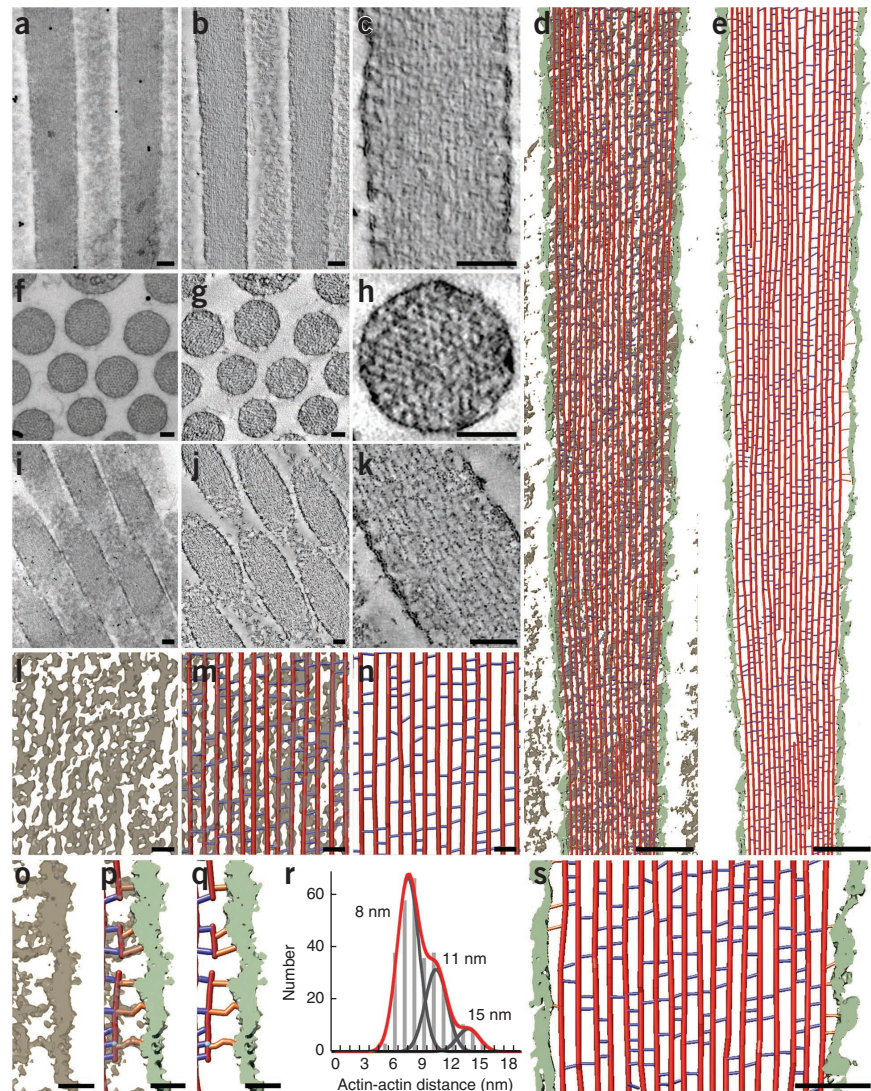
More proteins enriched in hair bundles may be encoded by as-yet-undiscovered deafness-associated genes. At least one-third of all deafness-associated genes are expressed in bundles, and, given ~400 human loci for nonsyndromic deafness<sup>21</sup>, another 100 bundle proteins might plausibly be associated with deafness. By identifying human homologs for bundle-enriched proteins and correlating genomic map locations with identified but uncloned deafness loci, we identified 13 new candidates for 8 deafness loci (Table 2).

### Actin cytoskeleton structure from electron tomography

To further validate the mass-spectrometric data, we used electron tomography<sup>22</sup> to count cytoskeletal structures in stereocilia from chick utricles (Fig. 3). We generated tomograms from stereocilia oriented longitudinally (Fig. 3a–c), transversely (Fig. 3f–h and Supplementary Fig. 6) and obliquely (Fig. 3i–k) to the plane of section. Each data set has distinct advantages for quantification. The longitudinal view allows us to follow individual actin filaments for long distances, but out-of-plane cross-linkers are less reliably detected owing to limited tilt-related data anisotropy. Transverse views allow ready measurement of actin-actin distances in all orientations, but the number of actin-actin links that can be detected is relatively small because of the ultrathin sections. Oblique views allow more reliable detection of out-of-plane cross-linkers, but these views are complicated by the section plane jumping from one actin filament to another. To interpret density maps obtained by electron tomography, we used two density thresholds to build simple ball-and-stick models. The use of two thresholds, which generated maximum and minimum estimates of cross-linker numbers, addressed difficulties in objectively thresholding density maps, which was complicated by reconstruction noise and possible staining inhomogeneity. We omitted out-of-plane cross-linkers in model building of our high-threshold (low estimate) rendered maps.

We measured in several independent subvolumes the total actin filament length, actin-actin spacing, number of actin-actin cross-linkers and number of actin-membrane connectors (Fig. 3d,e,i,s). A prototypical chick utricle stereocilium visualized by fluorescence and transmission electron microscopy was ~250 nm in diameter, ~5  $\mu$ m in length and hence ~0.2 fl in volume. Electron tomography indicated that there were ~210 actin filaments in a stereocilium of that diameter, or ~400,000 actin monomers in filaments (~3 mM).

**Figure 3** Electron tomography of chick stereocilia. (a–c) Tomogram from a stereocilium oriented longitudinally with respect to the plane of section. (a) Two-dimensional, 0° tilt projection image recorded for tomographic reconstruction. (b) Single ~0.8-nm slice of unfiltered three-dimensional reconstruction. (c) Single ~0.8-nm slice of bilaterally filtered density map. (d,e) Stereocilia model from longitudinal tomogram. Red lines represent actin, blue lines represent actin-actin cross-linkers, orange lines represent actin-membrane connectors and light green depicts membrane density. (d) Overview of stereocilia model overlaid on the surface-rendered density map (6.4 nm thick). (e) Overview of model alone and segmented membrane density. (f–h) Transverse stereocilia tomogram. (f) Two-dimensional, 0° tilt projection of transverse image recorded for tomographic reconstruction. (g) Single 0.8-nm slice of unfiltered three-dimensional reconstruction. (h) Single 0.8-nm slice of bilaterally filtered density map of transverse orientation, allowing precise measurements of actin-actin distances. (i–k) Oblique stereocilia tomogram. (i) Two-dimensional, 0° tilt projection of oblique image used for tomographic reconstruction. Stereocilia longitudinal axis is at an angle of ~18° with respect to sectioning plane. (j) Single 0.8-nm slice of unfiltered three-dimensional reconstruction. (k) Single 0.8-nm slice of bilaterally filtered three-dimensional reconstruction. (l,m) Scaled views of density and model in mid-shaft region; from longitudinal stereocilia orientation. (l) Density map only. (m) Model overlaid on the density map. (n) Model alone. (o–q) Close-up views of density map in a region adjacent to the membrane. (o) Density map only. (p) Model overlaid on the density map. (q) Model alone. (r) Histogram showing distribution of actin-actin distances at sites of cross-bridges. The data were fit with the sum of three Gaussians (red), with equal  $\sigma$  (width) for each. Individual fits for 8-, 11- and 15-nm peaks are shown in gray. (s) Close-up view of model. Scale bars: 100 nm in a–k, 20 nm in l–q, 50 nm in s.



(s) Close-up view of model. Scale bars: 100 nm in a–k, 20 nm in l–q, 50 nm in s.

Using the low threshold (upper limit) and averaging the data from six subvolumes per tomogram, we estimated  $62,000 \pm 1,000$  (longitudinal-orientation tomogram) and  $91,000 \pm 2,000$  (oblique-orientation tomogram) cross-linkers per prototypical stereocilium (mean  $\pm$  s.e.m.). The conservative lower-limit estimates with a high-density threshold, which also do not consider out-of-plane cross-linkers, were  $30,000 \pm 1,000$  and  $36,000 \pm 2,000$ . Assuming three cross-linkers for every 36 nm of actin filament<sup>23</sup>, the theoretical maximum is ~87,000.

We also counted actin-to-membrane connectors with electron tomography. The prototypical stereocilium has ~52 actin filaments adjacent to the plasma membrane; as a binding site should appear every 36 nm along each actin filament, each stereocilium could contain as many as 7,200 actin-membrane connectors. We counted  $7,300 \pm 1,100$  connectors per stereocilium with the low-density threshold and  $5,800 \pm 900$  using the high threshold (Fig. 3g–i).

### Stereociliary protein network

Focusing on the actin cytoskeleton, we identified potential interactions between hair-bundle proteins and depicted them using graph

theory<sup>24</sup> with spring-electrical modeling<sup>25</sup>, generating a mathematically defined, undirected graph that illustrates these relationships. We chose most of the major cytoskeletal proteins that were significantly enriched in hair bundles (Table 1) to seed the network. Searching the STRING (<http://string-db.org/>) and BioGRID (<http://thebiogrid.org/>) databases identified some interactions for these proteins; however, not all known interactions are in these or other protein-protein interaction databases. We therefore manually curated our protein interaction list (Supplementary Table 2) by searching PubMed for each protein in the network, allowing us to both validate interactions and identify additional ones. All interactions identified are given in Supplementary Table 3.

The network (Fig. 4 and Supplementary Fig. 7) highlights important hair-bundle proteins, as well as signaling molecules and ions. In most molecular networks, most nodes have only a few links but others—highly connected hubs—have many, which hold the sparsely linked nodes together<sup>26</sup>. For the 69 nodes with at least two interactions, the protein-interaction distribution data were fit well by a power law<sup>26</sup>, with  $P(k) \propto k^{-1.3}$ ,  $R = 0.79$  and  $P < 10^{-3}$ . The average clustering coefficient  $C_i = 2n_i/k_i(k_i - 1)$ , where  $n_i$  is the number of

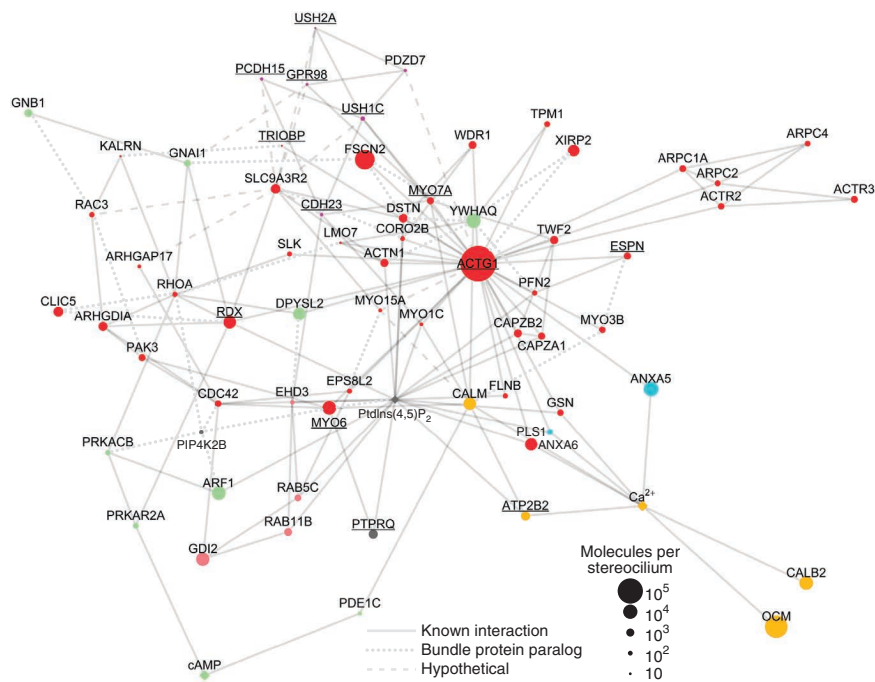


**Figure 4** Interaction network for hair-bundle proteins. Symbols (nodes) represent bundle proteins or second messengers; only nodes with two or more interactions are plotted, with the exception of OCM and CALB2. Underlined labels indicate deafness-associated proteins. Node colors indicate functional classification (same key as in **Fig. 2b**); node symbol size represents protein abundance in bundles.  $Ca^{2+}$ , PtdIns(4,5) $P_2$  and cyclic AMP are indicated by diamond node symbols. Solid links represent interactions validated with literature citations; **Supplementary Table 3** lists all interactions and evidence. Dotted links correspond to interactions involving paralogs of bundle proteins; dashed links represent hypothetical interactions (for example, SLC9A3R2 interactions from **Table 3**). The layout of the plot is controlled by the density of links between nearby nodes. The distribution of nodes and links in the plot is fit well by a power law, which indicates that the plot contains a few highly connected nodes (hubs) and many other less-connected nodes. **Supplementary Figure 7** reproduces this figure with each link hyperlinked to a PubMed reference supporting the interaction.

links connecting the  $k_i$  neighbors of node  $i$  to each other, represents how nodes interconnect<sup>26</sup>. The  $C_i$  value of 0.24 measured for our network indicates strong clustering<sup>27</sup>. Nodes with the largest numbers of links were actin (33 interactions), PtdIns(4,5) $P_2$  (20), SLC9A3R2 (12), CALM (9), RDX (8) and  $Ca^{2+}$  (8).

**RDX and SLC9A3R2**

RDX and SLC9A3R2, identified as hubs in the hair-bundle protein network, were each detected in chick utricle bundles by immunoblotting (**Fig. 5a** and **Supplementary Fig. 8**). We also found that SLC9A3R2 expressed in a human embryo kidney cell line (HEK293T) immunoprecipitated with RDX; SLC9A3R2 binds to activated

ERM proteins<sup>28</sup>, and binding was indeed stronger to RDX with a threonine-to-aspartate mutation that mimics the activating phosphorylation (**Fig. 5b** and **Supplementary Fig. 8**). In bullfrog stereocilia, RDX is activated by PtdIns(4,5) $P_2$  and phosphorylation is found in a narrow band above basal tapers, at the site of the ankle links<sup>5</sup>.

**Figure 5** Identification of RDX and SLC9A3R2 in hair bundles.

(a) Protein immunoblotting with purified hair bundles. Hair bundle lane represents bundles from 40 chick ears (~0.6  $\mu$ g total protein); agarose lane represents agarose equivalent to that in the bundles sample; epithelium lane represents utricle sensory epithelium from 4 chick ears (~10  $\mu$ g protein). Antibodies used are indicated at left. Both anti-RDX and anti-pERM (which recognizes phosphorylated ezrin, radixin and moesin) detected bands both at the expected size (~70 kDa) and at ~80 kDa (\*). (b) RDX-SLC9A3R2 interaction. Myc or hemagglutinin (HA) epitope-tagged chick wild-type RDX, T564D-RDX and SLC9A3R2 were expressed in HEK cells in the indicated combinations. Tagged SLC9A3R2 was immunoprecipitated, and associated RDX was detected by immunoblotting. (c) RDX and pERM immunocytochemistry. RDX and pERM colocalize except in the taper region (double arrows in bottom panel). Inset, magnification of apical surfaces of supporting and hair cells. pERM immunoreactivity is absent from bases of microvilli (MV), as in stereocilia (SC). Scale bar in **c** is 10  $\mu$ m and applies to **c-f**. (d) RDX and SLC9A3R2 immunocytochemistry. RDX and SLC9A3R2 overlap throughout the bundle, but SLC9A3R2 is more concentrated toward stereociliary bases (double arrows in bottom panel), including the tapers, than is RDX. (e) MYO7A immunocytochemistry. MYO7A is concentrated toward stereociliary tips and in a band above the taper region (\*). (f) RHOA immunocytochemistry. Staining is seen in stereocilia (arrow) and the kinocilium or the tallest stereocilia of the bundle (arrowheads). RHOA is also substantially enriched in hair cells over supporting cells.

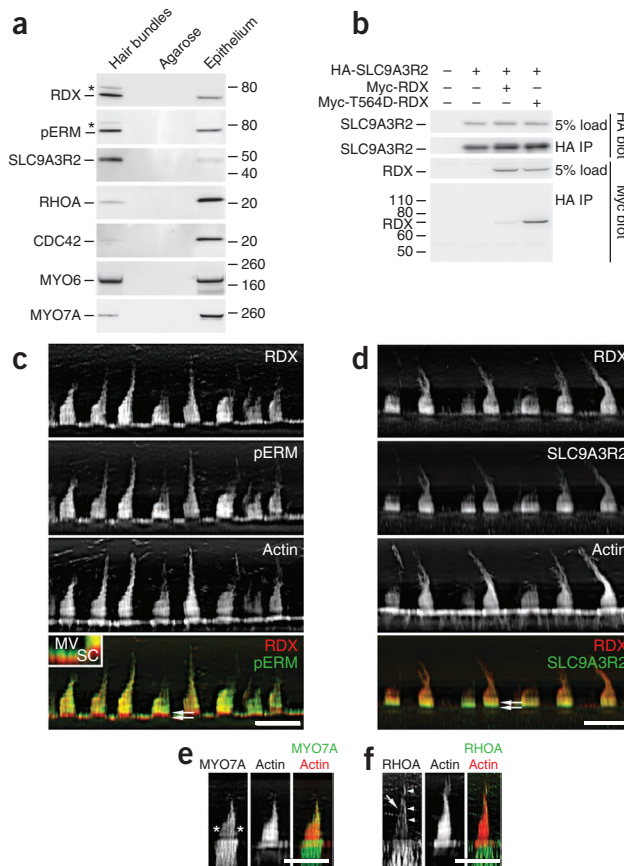


**Table 3 Candidate SLC9A3R2-binding proteins**

Identifier	Last 4 residues	Description	Protein symbol	BUN/UTR ratio
ENSGALP00000004315	STAL	Protocadherin-15	PCDH15	35
ENSGALP00000038711	MTFF	Harmonin (Usher syndrome 1C)	USH1C	22
ENSGALP00000000916	ETKL	Espin	ESPN	10
ENSGALP00000007402	ITEL	Cadherin-23	CDH23	3
ENSGALP00000004504	CTVF	Ras-related C3 botulinum toxin substrate 3	RAC3	2
ENSGALP00000015700	DTHL	Usherin (Usher syndrome 2A)	USH2A	2
ENSGALP00000023576	DTHL	G protein-coupled receptor 98	GPR98	1.3
ENSGALP00000018350	ETSL	ATPase, Ca <sup>2+</sup> transporting, plasma membrane 1 <sup>a</sup>	ATP2B1	1
ENSGALP00000015409	ESDL	Actinin, alpha 1 <sup>b</sup>	ACTN1	0.9
ENSGALP00000019939	LTLI	Cold inducible RNA binding protein	CIRBP	0.9
ENSGALP00000040234	PTGF	Casein kinase 1, alpha 1	CSNK1A1	0.9
ENSGALP00000003482	ATVL	Dmx-like 1	DMXL1	0.8
ENSGALP00000009572	STAL	Rho GTPase activating protein 17	ARHGAP17	0.4
ENSGALP00000015964	NTFF	Ribosomal protein L18a	RPL18A	0.3
ENSGALP00000009665	KTSL	Coatomer protein complex, subunit beta 1	COPB1	0.2
ENSGALP00000024331	DTEL	Tight junction protein 2 (zona occludens 2)	TJP2	0.2
ENSGALP00000007487	VLLI	CSE1 chromosome segregation 1-like	CSE1L	0.1
ENSGALP00000039286	QTEF	Family with sequence similarity 129, member B	FAM129B	0.1
ENSGALP00000019402	DTDL	Catenin (cadherin-associated protein), beta 1, 88 kDa	CTNNB1	0.08
ENSGALP00000017577	QTEL	Anterior gradient 3 homolog	AGR3	0.05
ENSGALP00000023016	PTTL	LIM and calponin homology domains 1	LIMCH1	0.04
ENSGALP00000019992	GTSL	Golgin A4	GOLGA4	0.02
ENSGALP00000012817	STCL	Laminin, beta 1	LAMB1	0.01
ENSGALP00000023309	ESDL	Actinin, alpha 2 <sup>b</sup>	ACTN2	NA
ENSGALP00000005687	ETSL	ATPase, Ca <sup>2+</sup> transporting, plasma membrane 2 <sup>a</sup>	ATP2B2	NA

We searched the C-terminal four amino acids of all chick bundle proteins for instances of XTXL (where X is any amino acid), XTXF, GVGL, ESDL, STHM and TLGA, all which bind to SLC9A3R2 (ref. 30). NA, not applicable.

<sup>a</sup>ATP2B1 and ATP2B2 are in the same protein group. Only the 'b' splice forms of these proteins bind PDZ domains; the splice form of ATP2B2 in hair bundles is 'a'. <sup>b</sup>ACTN1 and ACTN2 are in the same protein group.

Similarly, SLC9A3R2 and total RDX were concentrated in the bottom half of each stereocilium (Fig. 5c,d), and phosphorylated total ERM protein (pERM) was only found above stereociliary tapers (Fig. 5c). Likewise, pERM was concentrated in the upper half of supporting-cell microvilli (Fig. 5c, inset). Although MYO7A also appears in a band above basal tapers<sup>29</sup>, its distribution was distinct from those of RDX and SLC9A3R2 (Fig. 5e). Finally, we detected in hair bundles the Rho-family GTPases RHOA, RAC3 and CDC42, which control the actin cytoskeleton (Supplementary Table 1 and Fig. 5a,f).

When bound to RDX, the PDZ domains of SLC9A3R2 are available for binding; on the basis of consensus sequences for SLC9A3R2 ligands<sup>30</sup>, we identified 24 hair-bundle proteins as candidate binding partners, including CDH23, PCDH15, USH1C, USH2A and GPR98 (Table 3).

**DISCUSSION**

Here we used quantitative mass spectrometry to establish an extensive compendium of the proteins of vestibular hair bundles, available for browsing on the SHIELD website of inner-ear gene expression data sets (<https://shield.hms.harvard.edu/>). These data will allow us to systematically address two crucial topics for the cell biology of hair cells: construction of the bundle cytoskeleton during development, and composition and assembly of the transduction complex. By determining functional relationships between bundle proteins, investigating static and dynamic protein localization, measuring protein abundance and cataloging protein-protein interactions, we will gain a comprehensive understanding of how bundle proteins cooperate to make the bundle and carry out transduction.

**Actin cytoskeleton**

As expected given the structure of the stereocilium cytoskeleton, actin and actin-associated proteins were abundant in the mass spectrometry

data. We compared the tomography estimates to abundances of known actin-actin cross-linkers and actin-membrane connectors measured by mass spectrometry using the riBAQ method (Table 1). We detected three classes of cross-linkers: fascins (40,000 molecules per stereocilium of FSCN2, 1,300 FSCN1), plastins (5,500 PLS1, also known as fimbrin; 460 PLS2; 400 PLS3) and espins (710 ESPN and 90 ESPNL), similar to what we found previously<sup>31</sup>. Mass spectrometry thus estimates that each stereocilium has ~48,000 cross-linkers, in good agreement with the tomography estimates (33,000–77,000).

The ERM family, which cross-links membrane-protein complexes to actin at ~36-nm intervals, likely contributes most of the actin-membrane connectors. By mass spectrometry, EZR (ezrin), RDX and MSN (moesin) together totaled 6,800 molecules per stereocilium (Table 1), with RDX accounting for the majority; this value is within the range estimated by tomography (5,800–7,300).

Remaining actin-to-membrane connectors may be members of the myosin superfamily<sup>1</sup>. Mass-spectrometric quantification gave estimates of myosin abundance that corresponded well with independent measurements. By quantitative immunoblotting,

bullfrog bundles have >700 molecules per stereocilium of MYO6, >400 of MYO7A and 100 of MYO1C<sup>29</sup>; mass spectrometry estimated 6,600 chick MYO6, 250 MYO7A and ~50 each of MYO1C and the closely related MYO1H.

Actin polymerization in stereocilia, which is dynamic at least through late development<sup>32</sup>, is controlled by the myosin III and myosin XV families<sup>1</sup>. We detected 430 myosin III molecules per stereocilium, nearly all of which was MYO3B. Notably, the concentration of MYO3B was very close to that of its binding partner ESPN and that of PFN2, the profilin paralog that binds to ESPN.

We detected 50 molecules per stereocilium of MYO15A. Although we did not detect the MYO15A binding partner DFNB31, we found 130 molecules of EPS8L2 (EPS8-like 2); because its paralog EPS8 (epidermal growth factor receptor pathway substrate 8) binds the MYO15A-DFNB31 complex, EPS8L2 might partner with MYO15A in the vestibular system. Altogether we counted ~7,500 myosin molecules per stereocilium, which could account for remaining actin-to-membrane connectors.

Several other proteins also control polymerization of actin networks<sup>33</sup>. We detected five of seven subunits of the ARP2/3 complex, which mediates polymerization of branched actin networks; at 3 μM (~340 molecules per stereocilium), the ARP2-ARP3 complex is present at concentration similar to that in human neutrophils<sup>34</sup>. Because we did not detect any activating WASP/WAVE family members, however, the ARP2/3 complex likely is inactive in stereocilia. We did not detect any Ena/VASP family members, and although we detected one formin (DIAPH2) in one bundle experiment, its enrichment value suggested that it was a contaminant. Together these results suggest that control of actin-filament polymerization in late development involves only myosin-mediated mechanisms.

Although actin may not treadmill from tip to taper<sup>35</sup>, the stability of stereociliary actin filaments suggests that their barbed ends,



at stereociliary tips, are capped. If one barbed-end capper is present per filament and if filaments run the length of the stereocilium, there should be ~210 cappers per stereocilium. We detected two main cappers: ~700 CAPZ (capping protein) heterodimers per stereocilium and 950 TWF2 (twinfilin-2) molecules. The excess of cappers over actin filaments suggests that they compete for filament ends, which could occur differentially in longer and shorter stereocilia.

Pointed ends of stereociliary actin filaments progressively terminate to form stereociliary tapers, suggesting a systematic capping or depolymerization there. We did not detect tropomodulin, the best-characterized pointed-end capper<sup>36</sup>, nor did we detect taperin, a candidate pointed-end capper<sup>37</sup>. The pointed ends of stereociliary actin filaments either terminate on the taper membrane<sup>23</sup> or gather into the central rootlet material<sup>38</sup>; if the former, MYO6 could anchor the pointed ends to the membrane protein PTPRQ (protein tyrosine phosphatase, receptor type, Q)<sup>39</sup>, present at 1,500 copies per stereocilium, or if the latter, the rootlet component TRIOBP (TRIO and F-actin binding protein)<sup>40</sup> (detected in one experiment only) could cross-link filament ends to the rootlet.

At 4,600 molecules per stereocilium, XIRP2 (Xin-related protein 2) is the most abundant protein in hair bundles without an obvious role. Although most species' XIRP2 proteins contain >30 actin-binding Xin repeats, chick and rat bundle XIRP2 do not contain these domains (Supplementary Fig. 4b). However, XIRP2 is a paralog of the actin-binding protein LIMA1 (ref. 41), also known as EPLIN, suggesting that XIRP2 may nevertheless bind actin.

Network analysis highlighted the role of several other cytoskeletal proteins. The largest hair-bundle hub was actin, with 33 interactions; PtdIns(4,5)P<sub>2</sub> had 20 interactions, which was expected given its prominence in stereocilia<sup>5</sup> and actions in actin polymerization<sup>42</sup> and membrane targeting<sup>43</sup>. As is clear from co-clustering of the two hubs in the network map (Fig. 4), many bundle proteins bind both actin and PtdIns(4,5)P<sub>2</sub>; moreover, several bundle proteins not known to interact with actin do bind to PtdIns(4,5)P<sub>2</sub>, suggesting that the phospholipid may concentrate some membrane-associated proteins in stereocilia. Also prominent were CALM and Ca<sup>2+</sup>, with respectively 9 and 8 interactions; Ca<sup>2+</sup> entering stereocilia through transduction channels couples mechanotransduction to CALM-dependent enzyme activity.

RDX and SLC9A3R2 (2,000 molecules per stereocilium) had respectively 8 and 12 interactions, including a direct interaction between them that is facilitated by RDX phosphorylation. A major binding partner for RDX is thought to be CLIC5 (chloride intracellular channel 5)<sup>44</sup>, which can interconvert between cytosolic and transmembrane forms. At 2,400 molecules per stereocilium, CLIC5 could bind RDX molecules not bound by SLC9A3R2. RHOA, detected in stereocilia, induces translocation of CLIC4, a paralog of CLIC5, to the plasma membrane<sup>45</sup>; moreover, RHOA can activate RDX after preactivation by PtdIns(4,5)P<sub>2</sub> (ref. 46). RHOA may therefore both activate RDX and target its receptor to stereociliary membranes, providing a scaffold for other protein-protein interactions.

Other membrane proteins will interact with RDX through SLC9A3R2. Given the critical function of the paralog SLC9A3R1 in assembling microvilli<sup>47</sup>, we propose that SLC9A3R2 is necessary for assembling stereocilia. SLC9A3R1 is highly dynamic in microvilli<sup>48</sup>, suggesting that SLC9A3R2 complexes may be dynamic in stereocilia. Moreover, likely ligands for SLC9A3R2 are of known importance for bundle structure and function. USH2A and GPR98 are located at the ankle links<sup>1</sup>; RDX may anchor ankle links there through SLC9A3R2. SLC9A3R2 and RDX might also anchor the CDH23- and PCDH15-containing transient lateral links required for forming a cohesive bundle<sup>1</sup>.

## Other hair bundle proteins

Mechanotransduction molecules are rare in hair bundles; there is only one tip link and two active transduction channels per stereocilium<sup>1</sup>. Nevertheless, we detected ~20 molecules per stereocilium each of the tip link cadherins, CDH23 and PCDH15 (protocadherin 15), as well as 60 USH1C (harmonin) molecules, which cluster to anchor the upper end of a tip link<sup>1</sup>. Although the tip link of a single stereocilium should only contain two each of the cadherins, they are also present in the lateral links of developing bundles and in kinocilial links (Supplementary Fig. 4)<sup>1</sup>.

Our inability to detect other transduction proteins—such as the elusive transduction channel—likely arises from the limited dynamic range of mass spectrometry, rather than lack of sensitivity. In each mass spectrometry run, we matched ~10<sup>4</sup> spectra to chick peptides; because only 1–10 molecules of the transduction channel may be present for every 10<sup>6</sup> bundle molecules, substantial enrichment may be required to detect it above the background of actin and other cytoskeletal proteins.

Axonemal kinocilia are present in the hair-bundle preparation<sup>4</sup>; besides tubulin, we detected the axonemal dyneins DNAH5 and DNAH9, the radial spoke head molecules RSHL1, RSPH6A and RSPH9, the intraflagellar transport molecule IFT172 and the axonemal small GTPase ARL13B.

Diffusible Ca<sup>2+</sup> buffers were prominent; we estimated 63,000 OCM, 8,000 CALB2 (calretinin) and 7,300 CALM (calmodulin) per stereocilium, together corresponding to a total of ~2 mM Ca<sup>2+</sup> binding sites. The estimated CALM concentration (~60 μM) is nearly identical to the 70 μM estimated for bullfrog hair bundles by quantitative immunoblotting<sup>49</sup>. The membrane area of the prototypical stereocilium is ~4 μm<sup>2</sup>; if the density of the Ca<sup>2+</sup> pump in chick bundles is the same as in bullfrog (2,000 molecules μm<sup>-2</sup>; ref. 50), each stereocilium would have 8,000 Ca<sup>2+</sup> pumps. Mass spectrometry estimated significantly fewer, ~1,700 (mostly ATP2B2), perhaps because transmembrane peptides are not well detected in LC-MS/MS experiments.

## Conclusions

Many proteins enriched in hair bundles are encoded by deafness-associated genes, suggesting that other bundle-enriched proteins may be linked to deafness in the future. Mass spectrometry allows us to identify functionally important bundle proteins that have not yet been identified by genetics, such as proteins that carry out multiple functions in an organism and could have an embryonic lethal phenotype. Indeed, genetic screens for deafness likely miss ubiquitously expressed proteins with developmental roles; by contrast, the mass spectrometric approach can in principle identify any protein that contributes to maintenance and function of the hair bundle.

## METHODS

Methods and any associated references are available in the [online version of the paper](#).

**Accession codes.** Mass spectrometry data have been deposited to the ProteomeXchange Consortium via the PRIDE partner repository with data set identifier [PXD000104](#).

*Note: Supplementary information is available in the [online version of the paper](#).*

## ACKNOWLEDGMENTS

Mass spectrometry was carried out by the W.M. Keck Biomedical Mass Spectrometry Laboratory and The University of Virginia Biomedical Research Facility. We thank K. McDonald, R. Zalpuri and G. Min of the University of California Berkeley Electron Microscopy Laboratory for assistance with

high-pressure freezing and imaging; D. Jorgens provided mentoring in high-pressure freezing. We would like to thank A. Cheng, B. Carragher and C. Potter for help with electron microscopy data collection at the National Resource for Automated Molecular Microscopy, supported by US National Institutes of Health (NIH) National Center for Research Resources grant RR017573. For technical assistance, we acknowledge A. Snyder of the Advanced Light Microscopy Core at The Jungers Center (Oregon Health & Science University), supported by shared instrumentation grants S10 RR023432 and S10 RR025440 from the National Center for Research Resources (NIH). Work described here was supported by NIH grants K99/R00 DC009412 (J.B.S.), F32 DC012455 (J.F.K.), R01 DC002368 (P.G.B.-G.), R01 DC011034 (P.G.B.-G.), P30 DC005983 (P.G.B.-G.), R01 EY007755 (L.L.D.), P30 EY10572 (L.L.D.) and P01 GM051487 (M.A.).

**AUTHOR CONTRIBUTIONS**

J.-B.S. and P.G.B.-G. designed the overall approach and analysis. J.F.K. carried out immunoblotting and immunocytochemistry experiments of **Figures 2 and 5**, as well as **Supplementary Figures 2 and 4**; she also carried out quantitative immunoblots of **Figure 1**. J.-B.S. and J.M.P. prepared hair-bundle and epithelium samples for mass spectrometric analysis. A.H., Z.M., A.N.T. and M.A. carried out electron tomography and analyzed tomography data. N.E.S. and E.D.J. carried out mass spectrometry experiments. K.J.S. carried out immunocytochemistry experiments of **Supplementary Figure 4**. H.Z. carried out immunoprecipitation experiments of **Figure 5**. D.C. carried out the statistical analyses. P.G.B.-G. carried out mass spectrometry data analysis, with assistance from P.A.W. and L.L.D. The manuscript was written by P.G.B.-G.

**COMPETING FINANCIAL INTERESTS**

The authors declare no competing financial interests.

Published online at <http://www.nature.com/doi/10.1038/nn.3312>.

Reprints and permissions information is available online at <http://www.nature.com/reprints/index.html>.

1. Schwander, M., Kachar, B. & Müller, U. The cell biology of hearing. *J. Cell Biol.* **190**, 9–20 (2010).
2. Peng, A.W., Salles, F.T., Pan, B. & Ricci, A.J. Integrating the biophysical and molecular mechanisms of auditory hair cell mechanotransduction. *Nat. Commun.* **2**, 523 (2011).
3. Domon, B. & Aebersold, R. Options and considerations when selecting a quantitative proteomics strategy. *Nat. Biotechnol.* **28**, 710–721 (2010).
4. Shin, J.B. *et al.* Hair bundles are specialized for ATP delivery via creatine kinase. *Neuron* **53**, 371–386 (2007).
5. Zhao, H., Williams, D.E., Shin, J.B., Brugger, B. & Gillespie, P.G. Large membrane domains in hair bundles specify spatially constricted radixin activation. *J. Neurosci.* **32**, 4600–4609 (2012).
6. Donowitz, M. *et al.* NHERF family and NHE3 regulation. *J. Physiol. (Lond.)* **567**, 3–11 (2005).
7. Jones, S.M. & Jones, T.A. Ontogeny of vestibular compound action potentials in the domestic chicken. *J. Assoc. Res. Otolaryngol.* **1**, 232–242 (2000).
8. Gillespie, P.G. & Hudspeth, A.J. High-purity isolation of bullfrog hair bundles and subcellular and topological localization of constituent proteins. *J. Cell Biol.* **112**, 625–640 (1991).
9. Cox, J. *et al.* Andromeda: a peptide search engine integrated into the MaxQuant environment. *J. Proteome Res.* **10**, 1794–1805 (2011).
10. Cox, J. & Mann, M. MaxQuant enables high peptide identification rates, individualized p.p.b.-range mass accuracies and proteome-wide protein quantification. *Nat. Biotechnol.* **26**, 1367–1372 (2008).
11. Schwanhäusser, B. *et al.* Global quantification of mammalian gene expression control. *Nature* **473**, 337–342 (2011).
12. Tanaka, K. & Smith, C.A. Structure of the chicken's inner ear: SEM and TEM study. *Am. J. Anat.* **153**, 251–271 (1978).
13. Burnham, J.A. & Stirling, C.E. Quantitative localization of Na-K pump sites in the frog sacculus. *J. Neurocytol.* **13**, 617–638 (1984).
14. Kruger, R.P. *et al.* The supporting-cell antigen: a receptor-like protein tyrosine phosphatase expressed in the sensory epithelia of the avian inner ear. *J. Neurosci.* **19**, 4815–4827 (1999).
15. Schulte, B.A. & Adams, J.C. Immunohistochemical localization of vimentin in the gerbil inner ear. *J. Histochem. Cytochem.* **37**, 1787–1797 (1989).
16. Grati, M. *et al.* Localization of PDZD7 to the stereocilia ankle-link associates this scaffolding protein with the Usher syndrome protein network. *J. Neurosci.* **32**, 14288–14293 (2012).
17. Benjamini, Y. & Hochberg, Y. Controlling the false discovery rate: a practical and powerful approach to multiple testing. *J. R. Stat. Soc. Series B Stat. Methodol.* **57**, 289–300 (1995).
18. McKusick, V.A. Mendelian Inheritance in Man and its online version, OMIM. *Am. J. Hum. Genet.* **80**, 588–604 (2007).

19. Eppig, J.T. *et al.* The Mouse Genome Database (MGD): from genes to mice—a community resource for mouse biology. *Nucleic Acids Res.* **33**, D471–D475 (2005).
20. Spinelli, K.J. *et al.* Distinct energy metabolism of auditory and vestibular sensory epithelia revealed by quantitative mass spectrometry using MS2 intensity. *Proc. Natl. Acad. Sci. USA* **109**, E268–E277 (2012).
21. Steel, K.P. Genetic and environmental influences on hearing impairment. in *Genes and Common Diseases: Genetics in Modern Medicine* (eds. Wright, A.F. & Hastie, N.D.) 505–515 (Cambridge University Press, Cambridge, UK, 2007).
22. Auer, M. *et al.* Three-dimensional architecture of hair-bundle linkages revealed by electron-microscopic tomography. *J. Assoc. Res. Otolaryngol.* **9**, 215–224 (2008).
23. Tilney, L.G., Tilney, M.S. & DeRosier, D.J. Actin filaments, stereocilia, and hair cells: how cells count and measure. *Annu. Rev. Cell Biol.* **8**, 257–274 (1992).
24. Ma'ayan, A. Insights into the organization of biochemical regulatory networks using graph theory analyses. *J. Biol. Chem.* **284**, 5451–5455 (2009).
25. Fruchterman, T.M.J. & Reingold, E.M. Graph drawing by force-directed placement. *Softw. Pract. Exp.* **21**, 1129–1164 (1991).
26. Barabási, A.L. & Oltvai, Z.N. Network biology: understanding the cell's functional organization. *Nat. Rev. Genet.* **5**, 101–113 (2004).
27. Watts, D.J. & Strogatz, S.H. Collective dynamics of 'small-world' networks. *Nature* **393**, 440–442 (1998).
28. Fehon, R.G., McClatchey, A.I. & Bretscher, A. Organizing the cell cortex: the role of ERM proteins. *Nat. Rev. Mol. Cell Biol.* **11**, 276–287 (2010).
29. Hasson, T. *et al.* Unconventional myosins in inner-ear sensory epithelia. *J. Cell Biol.* **137**, 1287–1307 (1997).
30. Tonikian, R. *et al.* A specificity map for the PDZ domain family. *PLoS Biol.* **6**, e239 (2008).
31. Shin, J.B. *et al.* The R109H variant of fascin-2, a developmentally regulated actin crosslinker in hair-cell stereocilia, underlies early-onset hearing loss of DBA/2J mice. *J. Neurosci.* **30**, 9683–9694 (2010).
32. Rzadzinska, A.K., Schneider, M.E., Davies, C., Riordan, G.P. & Kachar, B. An actin molecular treadmill and myosins maintain stereocilia functional architecture and self-renewal. *J. Cell Biol.* **164**, 887–897 (2004).
33. Chhabra, E.S. & Higgs, H.N. The many faces of actin: matching assembly factors with cellular structures. *Nat. Cell Biol.* **9**, 1110–1121 (2007).
34. Higgs, H.N., Blanchoin, L. & Pollard, T.D. Influence of the C terminus of Wiskott-Aldrich syndrome protein (WASP) and the Arp2/3 complex on actin polymerization. *Biochemistry* **38**, 15212–15222 (1999).
35. Zhang, D.S. *et al.* Multi-isotope imaging mass spectrometry reveals slow protein turnover in hair-cell stereocilia. *Nature* **481**, 520–524 (2012).
36. Fischer, R.S. & Fowler, V.M. Tropomodulins: life at the slow end. *Trends Cell Biol.* **13**, 593–601 (2003).
37. Rehman, A.U. *et al.* Targeted capture and next-generation sequencing identifies C9orf75, encoding taperin, as the mutated gene in nonsyndromic deafness DFNB79. *Am. J. Hum. Genet.* **86**, 378–388 (2010).
38. Furness, D.N., Mahendrasingam, S., Ohashi, M., Fettiplace, R. & Hackney, C.M. The dimensions and composition of stereociliary rootlets in mammalian cochlear hair cells: comparison between high- and low-frequency cells and evidence for a connection to the lateral membrane. *J. Neurosci.* **28**, 6342–6353 (2008).
39. Sakaguchi, H. *et al.* Dynamic compartmentalization of protein tyrosine phosphatase receptor Q at the proximal end of stereocilia: implication of myosin VI-based transport. *Cell Motil. Cytoskeleton* **65**, 528–538 (2008).
40. Kitajiri, S. *et al.* Actin-bundling protein TRIOBP forms resilient rootlets of hair cell stereocilia essential for hearing. *Cell* **141**, 786–798 (2010).
41. Maul, R.S. *et al.* EPLIN regulates actin dynamics by cross-linking and stabilizing filaments. *J. Cell Biol.* **160**, 399–407 (2003).
42. Yin, H.L. & Janmey, P.A. Phosphoinositide regulation of the actin cytoskeleton. *Annu. Rev. Physiol.* **65**, 761–789 (2003).
43. Heo, W.D. *et al.* PI(3,4,5)P<sub>3</sub> and PI(4,5)P<sub>2</sub> lipids target proteins with polybasic clusters to the plasma membrane. *Science* **314**, 1458–1461 (2006).
44. Gagnon, L.H. *et al.* The chloride intracellular channel protein CLIC5 is expressed at high levels in hair cell stereocilia and is essential for normal inner ear function. *J. Neurosci.* **26**, 10188–10198 (2006).
45. Ponsioen, B. *et al.* Spatiotemporal regulation of chloride intracellular channel protein CLIC4 by RhoA. *Mol. Biol. Cell* **20**, 4664–4672 (2009).
46. Shaw, R.J., Henry, M., Solomon, F. & Jacks, T. RhoA-dependent phosphorylation and relocalization of ERM proteins into apical membrane/actin protrusions in fibroblasts. *Mol. Biol. Cell* **9**, 403–419 (1998).
47. Garbett, D., LaLonde, D.P. & Bretscher, A. The scaffolding protein EBP50 regulates microvillar assembly in a phosphorylation-dependent manner. *J. Cell Biol.* **191**, 397–413 (2010).
48. Garbett, D. & Bretscher, A. PDZ interactions regulate rapid turnover of the scaffolding protein EBP50 in microvilli. *J. Cell Biol.* **198**, 195–203 (2012).
49. Walker, R.G., Hudspeth, A.J. & Gillespie, P.G. Calmodulin and calmodulin-binding proteins in hair bundles. *Proc. Natl. Acad. Sci. USA* **90**, 2807–2811 (1993).
50. Dumont, R.A. *et al.* Plasma membrane Ca<sup>2+</sup>-ATPase isoform 2a is the PMCA of hair bundles. *J. Neurosci.* **21**, 5066–5078 (2001).



## ONLINE METHODS

**Animals.** Animal experiments reported here were approved by the Oregon Health & Science University Institutional Animal Care and Use Committee; the approval number was A684. All experiments began by killing the animal, which was done using methods approved by American Veterinary Medical Association Panel on Euthanasia.

**Preparation of samples for mass spectrometry.** Utricle hair bundles were purified from embryonic day 20–21 chicks using the twist-off method<sup>4,8</sup>. We estimated the fraction of epithelium protein accounted for by bundles using two independent methods. In the first, we divided the amount of bundle protein per utricle (16 ng; ref. 4), measured with a fluorescence protein assay, by the estimated recovery (~40%); this value was then divided by the protein per utricle (estimated here at  $2.4 \pm 0.2 \mu\text{g}$ ). This approach suggested bundle protein was 1.7% of the utricle's total protein. In the second method, we estimated the areas taken up by bundles and cell bodies in images of plastic sections of fixed, osmium-stained utricles examined by light microscopy. Using Fiji (<http://fiji.sc/>) to measure regions of interest, this method estimated that bundles make up  $1.8 \pm 0.6\%$  of the total protein in the utricle. Given the uncertainties in each, the methods suggested that bundles make up ~2% of the total protein in the utricle.

Separation of proteins by a short SDS-PAGE run before reduction, alkylation and trypsin digestion substantially increased sensitivity and reproducibility of detection in comparison to other methods<sup>31</sup>, in part because we could remove interfering polymers from the agarose used for bundle isolation. NuPAGE LDS sample buffer (Invitrogen) with 50 mM dithiothreitol was added to a combined final volume of 80  $\mu\text{l}$  per 100 utricles' worth of bundles; samples were heated to 70 °C for 15 min. Epithelial proteins were also solubilized with NuPAGE LDS sample buffer. Proteins were separated by running ~1 cm into a NuPAGE 4–12% Bis-Tris gel (1.5 mm  $\times$  10 well; one or two lanes per bundle sample); gels were rinsed with water, then stained with Imperial Protein Stain (Thermo Scientific). The 1 cm of gel with separated proteins was manually sliced into six pieces.

Gel pieces were transferred to siliconized tubes and washed and destained in 200  $\mu\text{l}$  50% methanol overnight. The gel pieces were dehydrated in acetonitrile, rehydrated in 30  $\mu\text{l}$  of 10 mM dithiothreitol in 0.1 M ammonium bicarbonate and reduced at room temperature (20–25 °C) for 0.5 h. The DTT solution was removed and the sample alkylated at room temperature (20–25 °C) for 0.5 h with 30  $\mu\text{l}$  of 50 mM iodoacetamide in 0.1 M ammonium bicarbonate. The reagent was removed and the gel pieces dehydrated in 100  $\mu\text{l}$  acetonitrile. The acetonitrile was removed and the gel pieces rehydrated in 100  $\mu\text{l}$  of 0.1 M ammonium bicarbonate. The pieces were dehydrated in 100  $\mu\text{l}$  acetonitrile, the acetonitrile removed and the pieces completely dried by vacuum centrifugation. The gel pieces were rehydrated in 20 ng/ $\mu\text{l}$  trypsin (Sigma-Aldrich T6567 proteomics grade, from porcine pancreas, dimethylated) in 50 mM ammonium bicarbonate on ice for 10 min. Any excess enzyme solution was removed and 20  $\mu\text{l}$  of 50 mM ammonium bicarbonate added. The sample was digested overnight at 37 °C and the peptides formed were extracted from the polyacrylamide in two 30- $\mu\text{l}$  aliquots of 50% acetonitrile, 5% formic acid. These extracts were combined and evaporated to 15  $\mu\text{l}$  for MS analysis. For the gel slice immediately adjacent to the agarose in the sample well, peptides were first purified away from interfering polymers on a SCX CapTrap from Bruker-Michrom (TR1/25109/35; size 0.5  $\times$  2 mm, bed volume 0.5  $\mu\text{l}$ ). The CapTrap was washed with 50  $\mu\text{l}$  of 1% acetic acid (void volume collected) and then eluted with 25  $\mu\text{l}$  1 M ammonium acetate into a separate microcentrifuge tube. The eluate was vacuum dried, then the sample reconstituted with 15  $\mu\text{l}$  of 3% acetic acid. A single experiment's worth of hair bundles or epithelium was analyzed by six LC-MS/MS runs, corresponding to the six gel pieces.

**Mass spectrometry data acquisition and analysis.** The LC-MS/MS system consisted of a Thermo Electron Orbitrap Velos ETD mass spectrometer system; the exceptional mass accuracy of the Orbitrap instrument allows for high resolution of peptide peak  $m/z$  (mass-to-charge ratio), which leads to high numbers of confident protein assignments. Peptides were introduced into the mass spectrometer with a Protana nanospray ion source, which was interfaced to a reversed-phase capillary column of 8 cm length  $\times$  75  $\mu\text{m}$  internal diameter, self-packed with Phenomenex C18 Jupiter of 10  $\mu\text{m}$  particle size. An extract aliquot (7.5  $\mu\text{l}$ ) was injected and peptides eluted from the column by an acetonitrile/0.1 M acetic acid gradient at a flow rate of 0.5  $\mu\text{l}/\text{min}$  over 1.2 h. The nanospray ion source was operated at 2.5 kV. The digest was analyzed using the data-dependent

capability of the instrument, acquiring—in sequential scans—a single full-scan mass spectrum in the Orbitrap detector at 60,000 resolution to determine peptide molecular weights, and 20 product-ion spectra in the ion trap to determine amino acid sequence.

MaxQuant version 1.2.2.5 software was used for protein identification and quantification<sup>10</sup>. The default contaminants file associated with the MaxQuant download was edited to remove entries known to be present in hair bundles (for example, actin) and to add additional impurities that entered the bundle-purification workflow (keratins, hemoglobins, egg white components). Nevertheless, alpha and beta hemoglobins, which appear in the preparation owing to contamination from red blood cells<sup>4</sup>, are expressed in chick utricle<sup>20</sup>, suggesting that they should not be fully dismissed as components of hair cells. Mass spectrometry data were searched against Ensembl version 66 (released February 2012) using Andromeda<sup>9</sup>; the Ensembl FASTA file was edited by replacing several sequences with longer or full-length sequences, including actin gamma 1 (NP\_001007825.1), actin beta (NP\_990849.1), fascin 1 (NP\_001171603), fascin 2 (NP\_001171209), ATP synthase beta (NP\_001026562.1), peptidylprolyl isomerase A (NP\_001159798.1), calbindin 2 (NP\_990647.1), PDZD7 (XP\_003641537.1), espin (XP\_417532.3) and CACNA2D2 (XP\_427707.3).

Protein identifications were reported with an FDR of 1%. Proteins identified with a single unique peptide are flagged in **Supplementary Table 1**. If a set of peptides for a protein was identical to or completely contained within that of another protein, MaxQuant groups those proteins together ('redundant groups'); the entry with the largest number of peptides was used to identify the redundant group. Redundant groups that shared more than 20% of their identified peptides were further grouped in our analysis ('shared-peptide groups'); the entry with the greatest intensity associated with it was used to identify the shared-peptide group. All mass spectrometry proteomics data, including raw data, MaxQuant output files and modified Ensembl FASTA database, have been deposited to the ProteomeXchange Consortium (<http://proteomecentral.proteomexchange.org/>) via the PRIDE partner repository<sup>51</sup> with the data set identifier PXD000104.

Annotation of the chicken genome is incomplete and occasionally wrong. For all proteins identified in the BUN preparation, we manually examined annotations of the chicken Ensembl entry and Ensembl-identified orthologs of other species, particularly mouse and human, to determine an appropriate description and symbol. Whenever possible, we chose the human ortholog's gene name, as determined by the Human Genome Organization, for a protein's symbol.

Gene Ontology annotation of the chicken genome is poor and, in many cases, was not useful for annotation of bundle proteins. Accordingly, we chose a simple, consistent set of ontology annotations to apply to all bundle proteins (see **Fig. 2b**). All proteins in the BUN preparation had one (and only one) of these ontologies assigned to it (**Supplementary Table 1**).

**Paralog identification.** Using data downloaded during October 2012 from the Chicken Ensembl database ([http://www.ensembl.org/Gallus\\_gallus/Info/Index/](http://www.ensembl.org/Gallus_gallus/Info/Index/)) BioMart tool, we also identified all paralogs in the chicken genome for each protein entry or group, calculating the average sequence identity for all paralogs matching to a protein or protein group. We also determined which paralogs for a protein or protein group were identified in the combined BUN and UTR data sets, as well as which were present in the group of all proteins that were significantly enriched at  $P < 0.05$  over the contamination fraction. These data are reported in **Supplementary Table 1**.

**Intensity-based mass-spectrometric quantification.** To quantify proteins, we used a label-free method that relies each detected peptide's ion-current signal in the mass spectrometer. As peptides elute from the liquid chromatograph, undergo ionization and are delivered to the mass spectrometer, the Orbitrap instrument we used measures their intensities, as well as measuring their mass-to-charge ratio with high resolution. Intensity depends both on the charge and amount of peptide delivered to the detector, although the efficiency of delivery varies widely from peptide to peptide because of variable recovery following liquid chromatography and differing degrees of ionization. Thus the relationship between intensity measured in the mass spectrometer and the amount of a peptide injected into the liquid chromatograph also varies, which limits quantification accuracy when standards for each protein are lacking. For example, hydrophobic peptides derived from transmembrane segments of integral membrane proteins are particularly poorly recovered, leading to reduced detection of this class of

proteins<sup>52</sup>. Moreover, mass spectrometers like the one we used are tuned to optimally detect peptides in a relatively narrow mass range, typically 6–30 amino acids, so proteins with an overabundance of short or long tryptic peptides are quantified less accurately than those with an average peptide. Nevertheless, measurement of protein abundance uses the sum of many peptide measurements, so with larger proteins—which generate many peptides—inter-peptide variability is averaged out and quantification accuracy is improved.

In the iBAQ algorithm<sup>11</sup>, the intensities of the precursor peptides that map to each protein are summed and divided by the number of theoretically observable peptides, which is considered to be all tryptic peptides between 6 and 30 amino acids in length. This operation converts a measure that is proportional to mass (intensity) into one that is proportional to molar amount (iBAQ). The release of the MaxQuant<sup>10</sup> we used (version 1.2.2.5) reports for each identified protein both its summed intensity and its iBAQ value.

To determine absolute amounts of each protein in stereocilia, we generated a normalized measure of molar abundance, relative iBAQ (riBAQ). We first removed from the analysis all contaminant proteins that entered our sample-preparation workflow, which include keratins (from human skin), hemoglobins (from blood), egg white proteins (for example, ovalbumin) and trypsin. We then divided each remaining protein's iBAQ value by the sum of all non-contaminant iBAQ values, generating an riBAQ value for each protein:

$$\text{riBAQ} = \frac{\text{iBAQ}_i}{\sum_{i=1}^n \text{iBAQ}_i} \quad (1)$$

For iBAQ validation experiments, we spiked one-fifth of a vial of UPS2 standard proteins (Universal Proteomics Standard 2; Sigma-Aldrich) into 25  $\mu\text{g}$  (~500 pmol total) of the *E. coli* extract. Each experiment thus included 48 human proteins, eight each at 10 pmol, 1 pmol, 100 fmol, 10 fmol, 1 fmol and 100 amol. We carried out four independent experiments using methods identical to those for hair bundles and utricular epithelia, including a 1-cm SDS-PAGE separation that was followed by slicing the gel into six pieces; reduction, alkylation and trypsin proteolysis; LC-MS/MS using the Orbitrap mass spectrometer; and MaxQuant analysis with riBAQ determination.

For quantitative immunoblot validation of riBAQ values, BUN and UTR samples were loaded into 10- or 15-well Novex NuPAGE Bis-Tris 4–12% gels, along with dilutions of purified protein standards, and separated by SDS-PAGE. Protein standards were CALM (bovine brain; EMD Millipore), ANXA5 (recombinant, from chicken; ImmunoTools GmbH), MYO1C (recombinant, from rat; gift of L. Coluccio, Boston Biomedical Research Institute) and FSCN2 (recombinant, from human; USCN Life Sciences). Five dilutions between 1 and 200 ng were used for CALM and ANXA5 standard curves, four dilutions between 0.01 and 1 ng for MYO1C and four dilutions between 1.25 and 10 ng for FSCN2. SDS-PAGE and immunoblotting were carried out essentially as described previously<sup>4,31</sup>. Band intensities were measured using Fiji imaging software and linear regression analysis was carried out to determine the amount of each protein (ng per ear) in the bundle and epithelium samples. Three experiments were carried out for each standard protein. To estimate the mole fraction of each protein, the estimate of ng per ear was converted to mol per ear, then was divided by the number of moles of total protein per ear. We estimated moles of protein per ear by dividing the amount of protein per ear's worth of bundles or epithelium, then dividing by the average molecular mass for all proteins in each sample, which was weighted by the mole fraction estimated by mass spectrometry (46 kDa for bundles, 56 kDa for epithelium).

**Statistical analysis.** Fisher's exact test was used to determine the significance of the increased numbers of deafness-associated proteins in the hair bundle samples. Permutation tests were employed to test whether the mean values of  $\log_2(\text{BUN riBAQ}/\text{UTR riBAQ})$  were significantly greater than the corresponding contamination fraction of  $\log_2(0.20)$ . Exact *P* values were computed and adjusted for multiple test corrections by the false discovery rate<sup>17</sup>. All computations were done by using the exactRankTests package in the R statistical computing environment.

**Electron microscopy sample preparation and tomography.** We used high-pressure freezing and freeze substitution<sup>53</sup> to optimally preserve osmotically sensitive samples. Chick utricle epithelia were dissected in chick saline

(155 mM NaCl, 5 mM KCl, 5 mM D-glucose and 10 mM 4-(2-hydroxyethyl)-1-piperazineethanesulfonic acid (HEPES)) containing 0.1 mM  $\text{CaCl}_2$ . The tissue was fixed for 2 h at room temperature (20–25 °C) in 3% glutaraldehyde (Electron Microscopy Sciences), 0.2% tannic acid, 100 mM KCl, 5 mM  $\text{MgCl}_2$  and 20 mM 3-(*N*-morpholino)propanesulfonic acid (MOPS) at pH 6.8, then washed three times for 5 min each at room temperature (20–25 °C) in the same solution without glutaraldehyde and tannic acid.

Samples were stained with 1%  $\text{OsO}_4$  in 0.1 M sodium phosphate buffer for 1 h on ice, followed by three rinses with 0.1 M sodium phosphate buffer and three more rinses with deionized water. Subsequent staining was carried out with 2% aqueous uranyl acetate at room temperature (20–25 °C) for 1 h, followed immediately by three rinses with deionized water. Samples were coated with a 20% glycerol cryoprotectant and frozen using a Bal-Tec HPM 010 high pressure freezer. Thereafter, freeze substitution was performed using a freeze substitution mix containing 0.1% uranyl acetate in 100% acetone. Epon-araldite resin embedding and infiltration was carried out as described<sup>22</sup>. Sections were cut at 70 or 120 nm for screening or for tomography, respectively. Thin sections, nominally 120 nm in thickness, were placed on  $2 \times 1$  mm oval-hole copper-rhodium grids with 0.6% Formvar coating for imaging and decorated with 10 nm or 15 nm gold fiducial markers for tomography. For greater stability upon beam exposure and to minimize charging, a thin film of carbon was deposited on grids containing sections using a Denton Vacuum system (DV-502). Initial screening and tomography was primarily done with JEOL1200-EX (TEM only), Philips CM200 FEG and FEI Tecnai F20 electron microscopes, whereas analyzed tilt series were collected using an FEI Tecnai T12 LaB6 electron microscope operated at 120 kV.

Images were recorded with a Gatan MegaScan Model 794/20 2K CCD (JEOL1200-EX), a Gatan First Light 4K CCD (CM200), a Tietz F415 4K CDD (F20) or a Gatan 1000 2,048  $\times$  2,048-pixel CCD camera (T12). Tomograms for quantification were collected using ~0.8  $\mu\text{m}$  underfocus at a nominal 13,500 $\times$  magnification, corresponding to a pixel size of 0.8 nm at the specimen level. Dual-axis tilt series were recorded at 1° intervals for angles of up to  $\pm 65^\circ$ . Projections were aligned and reconstructed into a three-dimensional volume with the software package IMOD<sup>54</sup>. Resulting maps were processed either with three iterations of a bilateral filter using PRIISM<sup>55</sup> or with successive rounds of smoothing, diffusion, or median filtering using the Clip program in IMOD. Segmentation and interactive simplified model building was done using UCSF Chimera<sup>56</sup>. The simplified model showing actin filaments, cross-linkers and connectors deliberately used cylinders smaller in diameter than their respective structures to allow adequate display of the cross-linkers and connectors.

**Stereociliary protein network.** The protein interaction data in **Supplementary Table 2** can be represented in the form of a graph  $G = \{N, L\}$ , where the set of nodes *N* correspond to bundle proteins and links *L* correspond to specific protein interactions. Two vertices *n* and *m* form an edge of the graph if  $\{n, m\} \in L$ ; because in our data  $\{n, m\} \in L$  implies  $\{m, n\} \in L$ , the graph is undirected and is drawn with line segments rather than arrows. To visualize the interrelationships between these interactions, they are displayed in a drawing (a graph, in the mathematical sense). To represent the interactions aesthetically, link crossings were minimized and spacing between nodes was kept relatively even. We used a straight-edge drawing algorithm, spring-electrical embedding<sup>25</sup>, which minimizes the energy of a physical model of the graph in two dimensions. Spring-electrical embedding uses two forces. The 'attractive force'  $f_a = d_{ij}^{-2}/K$  between adjacent nodes is proportional to the Euclidian distance between them ( $d_{ij}$ ); *K* is a spring-like constant that maintains the optimal distance between nodes. The 'electrical force' (repulsive) is global and inversely proportional to the Euclidian distance between nodes:  $f_r = K^2/d_{ij}$ . The layout of the graph vertices is then determined by minimizing the energy function described by these two forces<sup>25</sup>. These modeling rules draw together nodes with similar interactions and disperse unrelated ones, thus clustering related proteins, which may carry out similar roles in bundles. The spring-electrical embedding algorithm is implemented in Mathematica 8 (Wolfram Research; <http://www.wolfram.com/mathematica/>), which we used to generate the network figure.

**Antibody methods.** Primary antibodies were as follows: for ANXA5, polyclonal anti-chick ANXA5 from G. Richardson (University of Sussex); for alpha-tubulin, Sigma-Aldrich DMA1; for ATP1A1, Developmental Studies Hybridoma Bank a5; for ATP2B2, F2a (ref. 50); for ATP5A1, BD Transduction 612516; for CALM,

Millipore 05-173; for CDC42, Cell Signaling 2466 (11A11); for CDH23, C2367 goat anti-CDH23 EC15/16 junction (raised against CATRPAPPDRERQ by Genemed Synthesis, Inc.); for CKB, rabbit anti-chBCK from T. Wallimann (ETH Zürich); for CTNNB1, BD Transduction Labs 610154; for DSTN, anti-ADF/cofilin from J. Bamberg (Colorado State University); for ENO1, Santa Cruz H-300; for ESPN, anti-espinn from S. Heller (Stanford University) and pan-espinn from B. Kachar (NIH); for FSCN2, anti-CYTLEFKAGKLAFLKD (ref. 31); for GAPDH, Chemicon MAB374; for HSPA5 (GRP78), Abcam ab32618; for KIAA1211, rabbit anti-CVSTEPAWLALAKRKAKAWSD (produced for us by Genemed Synthesis, Inc.); for MDH2, Sigma-Aldrich HPA019714; for MYO1C, antibody 2652 (ref. 57); for MYO1H, rabbit G5991 anti-chick MYO1H C-terminal 15 kDa (produced for us by Genemed Synthesis, Inc.); for MYO3A, QHF anti-*Xenopus laevis* MYO3A C-terminal 22 amino acids (from B. Burnside, University of California, Berkeley); for MYO3B, rabbit anti-GDWIRKPLYGLFQYNSSMIGLES LC (produced for us by Genemed Synthesis, Inc.); for MYO7A, 138-1 (Developmental Studies Hybridoma Bank); for PCDH15, G19 anti-tip link antigen<sup>58</sup>; for PRKAR2A, Santa Cruz M-20; for PTPRJ, monoclonal antibody D37 (ref. 14); for RDX, Abnova H00005962-M06 (1D9); for pERM, Cell Signaling 3149 (41A3); for RHOA, Cell Signaling 2117 (67B9); and for talin, Sigma-Aldrich 8D4. We raised polyclonal sera against a mixture of two chicken SLC9A3R2 peptides (CHSDLQSPGKESEDGDSEK and CQRHSHSFSSSRKDLNGQKE). Antibodies to MYO6 were obtained from J. Kendrick-Jones (MRC Laboratory of Molecular Biology). We also used anti-SLC9A3R2 (anti-NHERF2) 2331B (from M. Donowitz; Johns Hopkins University) for immunoblotting.

For immunoblotting, utricles were dissected from day 20–21 chick embryos in cold, oxygenated chicken saline containing 4 mM CaCl<sub>2</sub>, and otolithic membranes were removed without protease treatment. SDS-PAGE and immunoblotting were carried out essentially as described previously<sup>4,31</sup>. Primary antibodies were used at 1:1,000, except anti-CALM (1:500). All secondary antibodies were diluted 1:10,000.

For immunoprecipitation, RDX and SLC9A3R2 were cloned from chicken utricle cDNA into expression vectors with respectively Myc and HA epitope tags. Proteins were expressed for 24 h in HEK293T cells using Effectene (Qiagen) transfection. Cells were lysed using a probe sonicator with PBS containing 1% Triton X-100, 0.5% NP40 and protease inhibitors; the extract was centrifuged at 16,000g for 15 min. The supernatant was removed and 300 µl was incubated with anti-HA-agarose (20 µl 50% slurry; Sigma A2095) overnight at 4 °C. Immunoprecipitates were washed and proteins were eluted with SDS sample buffer. SDS-PAGE and immunoblotting were carried out essentially as above.

For immunocytochemistry, dissected utricles were fixed for 25 min in 4% formaldehyde (Electron Microscopy Sciences) in chicken saline. Organs were rinsed in PBS, permeabilized for 10 min in 0.5% Triton X-100 in PBS and blocked for 2 h in 2% bovine serum albumin, 5% normal goat serum in PBS. Organs were incubated overnight at 4 °C with primary antibodies diluted in blocking solution (1:250 dilution for all primary antibodies except anti-SLC9A3R2 and anti-RDX, both at 1:500), then rinsed three times for 10 min each. Organs were then incubated for 3–4 h in blocking solution with 1:1,000 Alexa Fluor secondary antibodies and 0.4 U/ml Alexa Fluor 488 Phalloidin (Molecular Probes, Invitrogen). Organs were then rinsed three times for 20 min each and mounted on slides in Vectashield (Vector Laboratories) using one Secure-Seal spacer (eight wells, 0.12 mm deep, Invitrogen).

Images were acquired on an Olympus Fluoview FV1000 laser scanning confocal microscope system with AF10-ASW 3.0 acquisition software, using a 60× 1.42 NA Plan Apo objective with 3× zoom and 0.2-µm z-steps. Confocal images were deconvolved with the optical transfer function optimized for that objective using an iterative algorithm of ten iterations. The histogram was adjusted for the most positive image and applied to all the other images for consistency before saving the images as 24-bit merged TIFF files. All z-stacks were processed using Fiji (<http://fiji.sc/>); the Reslice function was used to generate an x-z slab of the stack.

51. Vizcaíno, J.A. *et al.* The Proteomics Identifications database: 2010 update. *Nucleic Acids Res.* **38**, D736–D742 (2010).
52. Barrera, N.P. & Robinson, C.V. Advances in the mass spectrometry of membrane proteins: from individual proteins to intact complexes. *Annu. Rev. Biochem.* **80**, 247–271 (2011).
53. Sosinsky, G.E. *et al.* The combination of chemical fixation procedures with high pressure freezing and freeze substitution preserves highly labile tissue ultrastructure for electron tomography applications. *J. Struct. Biol.* **161**, 359–371 (2008).
54. Kremer, J.R., Mastronarde, D.N. & McIntosh, J.R. Computer visualization of three-dimensional image data using IMOD. *J. Struct. Biol.* **116**, 71–76 (1996).
55. Chen, H., Clyborne, W.K., Sedat, J.W. & Agard, D.A. Prism: an integrated system for display and analysis of 3-D microscope images. *Proc. SPIE* **1660**, 784–790 (1992).
56. Pettersen, E.F. *et al.* UCSF Chimera—a visualization system for exploratory research and analysis. *J. Comput. Chem.* **25**, 1605–1612 (2004).
57. Dumont, R.A., Zhao, Y.D., Holt, J.R., Bahler, M. & Gillespie, P.G. Myosin-I isozymes in neonatal rodent auditory and vestibular epithelia. *J. Assoc. Res. Otolaryngol.* **3**, 375–389 (2002).
58. Goodyear, R.J. & Richardson, G.P. A novel antigen sensitive to calcium chelation that is associated with the tip links and kinocilial links of sensory hair bundles. *J. Neurosci.* **23**, 4878–4887 (2003).